

Investigation of Rechargeable Calcium Metal-Selenium Batteries Enabled by Borate-Based Electrolytes

Sanghyeon Kim,* Nathan T. Hahn, Timothy T. Fister, Noel J. Leon, Xiao-Min Lin, Haesun Park, Peter Zapol, Saul H. Lapidus, Chen Liao, and John T. Vaughey*



Cite This: *Chem. Mater.* 2023, 35, 2363–2370



Read Online

ACCESS |



Metrics & More

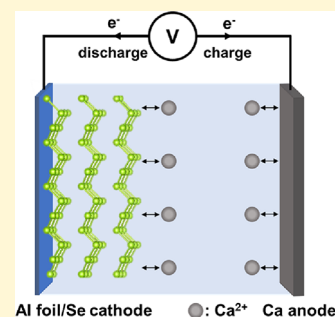


Article Recommendations



Supporting Information

ABSTRACT: Calcium-ion batteries (CIBs) are a promising next-generation energy storage system given the low redox potential of calcium metal and high abundance of calcium compounds. For continued CIB development, the discovery of high energy density calcium ion cathodes is needed to achieve practical energy density values. Here, we report on the use of elemental Se as a promising candidate for a high-capacity cathode material for CIBs that operates via a conversion mechanism in a Ca metal battery at room temperature. The Se electrodes demonstrate a reversible specific capacity of 180 mA h g⁻¹ with a discharge plateau near 2.0 V (vs Ca²⁺/Ca) at 100 mA g⁻¹ using an electrolyte based on the salt calcium tetrakis(hexafluoroisopropoxy)borate (Ca(B(hfip)₄)₂) in 1,2-dimethoxyethane (DME) and Ca metal. The reversible electrochemical reaction between calcium and selenium is investigated using operando synchrotron-based techniques and the possible reaction mechanism discussed.



1. INTRODUCTION

Although lithium-ion batteries (LIBs) have long been the dominant energy storage system for portable devices and electric vehicles,^{1,2} concerns regarding long-term availability of the active material components and the increasing demand for lower costs have led to an intensive search for new beyond lithium-ion technologies.^{3–5} Among beyond lithium chemistries, CIBs are particularly promising alternatives to LIBs due to the low reduction potential of calcium (−2.87 V vs standard hydrogen electrode), its high elemental abundance (fifth most abundant element in the earth's crust), and the high energy density of a calcium metal anode (Ca has a high volumetric capacity of 2073 mA h cm⁻³).^{6,7} However, the development of CIBs has been hampered by the lack of functional electrode materials and suitable electrolytes that enable reversible calcium plating and stripping. The importance of electrolytes was highlighted by recent reports highlighting advances in reversible calcium plating and stripping.^{8–12}

Recently, the new salt Ca(B(hfip)₄)₂ in the DME electrolyte was reported. Ca(B(hfip)₄)₂-based electrolytes represent the state of the art due to their exhibited high ionic conductivity (~8 mS cm⁻¹), high oxidative stability up to 4.5 V vs Ca²⁺/Ca, efficient Ca stripping and plating, and good chemical compatibility with both the Ca metal anode and cathode. Together, these attributes fulfill most of the prerequisites needed for a Ca metal battery electrolyte with the formation of a passivating layer on the Ca metal supporting prolonged cycling.^{10,11} The electrochemical properties of Ca(B(hfip)₄)₂-based electrolytes have opened up a wide array of possible cathode materials, including non-intercalation materials, that can be used with a Ca metal anode to create high energy

density Ca-based batteries.^{13–16} Even though the structural integrity of intercalation materials can favor long cycle life, the specific capacities observed are limited to an apparent maximum of 0.5 Ca per transition metal cation. On the other hand, conversion electrodes can provide high specific capacities by utilizing all possible redox states of the metal to be components of high energy density CIBs.

Among conversion cathode materials reported for Ca metal batteries, those based on sulfur have the highest theoretical capacity and possibly the lowest cost.^{13,14,17,18} However, like the Mg–S system, the energy storage mechanism for the Ca–S system also suffers from capacity fade due to a polysulfide shuttle and sluggish kinetics due to the insulating nature of CaS.^{13,14,19–23} Additionally, the discharge reaction is expected to have a high activation energy barrier due to the strong ionic bonds between the Ca²⁺ and S²⁻ ions and poorly defined diffusion pathways in the dense rocksalt-type lattice.

Because of the above mentioned issues associated inherently with sulfur cathodes, alternative materials that operate by a conversion mechanism should be considered to overcome some of these obstacles. A candidate that should operate by the same mechanism is elemental selenium, the element below sulfur in group 6A of the periodic table. Compared to sulfur, a reported advantage of selenium-based systems is that the

Received: November 8, 2022

Revised: February 12, 2023

Published: March 8, 2023



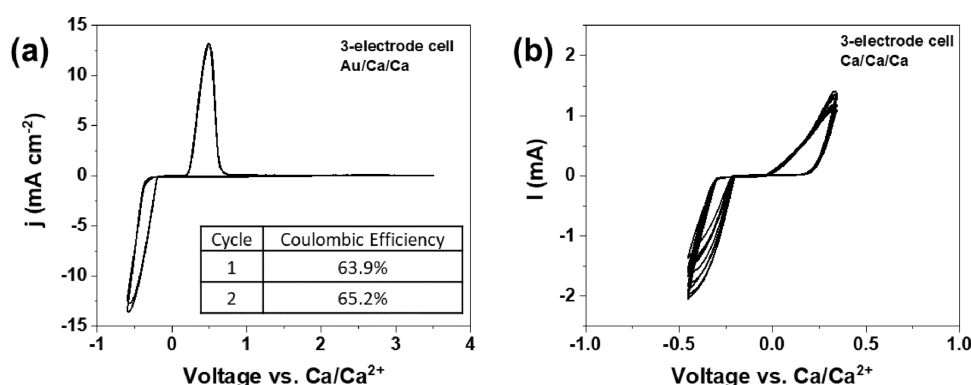


Figure 1. Cyclic voltammetry of a $\text{Ca}(\text{B}(\text{hfip})_4)_2$ in the DME electrolyte with (a) Au (two cycles) and (b) Ca working electrodes (10 cycles). Ca rods were used as counter and reference electrodes. Cyclic voltammetry was run at a 50 mV s^{-1} scan rate.

shuttling reaction for Se-based electrodes has a much higher dependence on the electrolyte formulation used than comparable sulfur systems, thus allowing for the possibility of improved Coulombic efficiencies.^{24,25} In addition, the larger size of the selenide anion and its more diffuse charge result in longer Ca–Se bonds in the end products and can lead to a more kinetically viable reversible reaction pathway on charging, with a theoretical capacity of 678 mA h g^{-1} , assuming that 1 mol of Ca can fully react with 1 mol of Se. While a recent paper examined the Ca–Se energy storage couple using activated carbon cloth as a counter/reference electrode,²⁶ our work extends that recent study to electrolytes more specifically designed for alkaline earth-based systems and creates a true full cell by utilizing a metallic calcium anode.

In this study, the physical and electrochemical properties of a Ca–Se full cell are demonstrated using a non-aqueous $\text{Ca}(\text{B}(\text{hfip})_4)_2$ -based electrolyte. The Se electrode exhibits a reversible specific capacity of 180 mA h g^{-1} at a discharge voltage of 2.0 V (vs Ca^{2+}/Ca) and a current of 100 mA g^{-1} at room temperature. This current equates to a reversible reaction involving 0.27 mol of Ca^{3+} per selenium. The electrochemical reaction mechanism between Ca and Se was investigated using several operando X-ray synchrotron techniques including high-resolution X-ray diffraction (XRD), X-ray absorption spectroscopy (XAS), and energy-dispersive X-ray spectroscopy (EDS) to better understand the structural and oxidation state and compositional changes associated with the electrochemical reactions.

2. EXPERIMENTAL SECTION

2.1. Material Preparation. Selenium powder (99.99%) was purchased from Sigma-Aldrich and used without further treatment. The Se/activated carbon composites were created using the as-received Se and activated carbon with a mass ratio of 1:1 and mixed using a mortar and pestle. The mixture was heated at $300 \text{ }^\circ\text{C}$ for 2 h under Ar gas flow for Se impregnation; the melting point of selenium was $221 \text{ }^\circ\text{C}$. Calcium selenide powder (CaSe , 99.9%) was purchased from Xi'an Function Material and used without further treatment.

2.2. Electrolyte and Electrode Preparation. All electrolyte handling was done inside a glovebox with water and oxygen levels below 1 and 0.1 ppm, respectively. The DME solvent was purchased from Sigma-Aldrich, distilled over sodium, and stored over activated alumina and 3A molecular sieves prior to use, and its measured water level was below 5 ppm. Synthetic reagents $\text{Ca}(\text{BH}_4)_2 \cdot 2\text{THF}$ and hexafluoroisopropanol (99.9%) were purchased from Sigma-Aldrich, and the hexafluoroisopropanol was dried over activated 3A molecular sieves. $\text{Ca}(\text{B}(\text{hfip})_4)_2$ salt was synthesized using a previously reported method.^{10,11} $\text{Ca}(\text{B}(\text{hfip})_4)_2$ electrolytes were prepared by dissolving

the recrystallized $\text{Ca}(\text{B}(\text{hfip})_4)_2$ solvate in DME to yield the desired electrolyte concentration. The final electrolyte concentrations were calculated from solution volume instead of solvent volume alone due to the significant volume contributions from the salts used. The cathode slurry was made with 60 wt % Se/activated carbon composites, 20 wt % carbon black (Timcal Super C45), and 20 wt % polyvinylidene fluoride (PVDF) with *n*-methyl-2 pyrrolidinone (NMP) (anhydrous 99.5%, Sigma-Aldrich) as a solvent. The mixture prepared by using a mortar and pestle was cast onto a carbon-coated Al foil. The electrodes were dried at $75 \text{ }^\circ\text{C}$ in air followed by drying at $80 \text{ }^\circ\text{C}$ under vacuum for 3 h.

2.3. Electrochemical Measurements. Ca metal batteries were assembled in Swagelok-type cells in a glove box under an Ar atmosphere. Ca metal chips (ACI Alloys), glass microfiber filters (Whatman 1825-055), and 0.2 M $\text{Ca}(\text{B}(\text{hfip})_4)_2$ in DME were used as counter electrodes, separators, and electrolytes, respectively. Both sides of the Ca metal were polished to remove the oxidized layer until the surface became shiny. Galvanostatic discharge–charge tests were conducted using a series 4000 Maccor cyclor or VMP3 potentiostat (Bio-Logic) over a voltage range of $1.6\text{--}3.5 \text{ V}$ versus Ca^{2+}/Ca at room temperature. Current densities and specific capacities were determined based on the mass of active materials (Se). Capacity variation from sample to sample was about 10%.

2.4. Material Characterization. Synchrotron XRD measurements were conducted at sector 11IDB and 11BM of Advanced Photon Source (APS) at Argonne National Laboratory (ANL). CaSe powder was put in a Kapton capillary and sealed by epoxy glue in a glove box to prevent air exposure for ex situ XRD measurement. Se K-edge XAS measurements were performed at sector 10BM at APS at ANL in transmission mode using elemental Se as the energy reference. The CaSe standard sample was covered with Kapton tape to protect it from air exposure. The XAS data were processed using the Athena software package. EDS was conducted using a Jeol JCM-6000 plus scanning electron microscope equipped with an EDS detector. EDS data were taken at 1000 \times magnifications to avoid local inhomogeneity. For ex situ sample preparation, the cells were disassembled after discharge and charge, and electrodes were washed with acetonitrile twice and dried in a glove box. The weight content of selenium in the final Se/activated carbon composites was measured by TGA using a Mettler Toledo 851e system under a nitrogen environment. The sample was stabilized at $25 \text{ }^\circ\text{C}$ for 10 min before ramping up to $800 \text{ }^\circ\text{C}$ with a heating rate of $10 \text{ }^\circ\text{C min}^{-1}$. For in situ cells, Kapton tape and a Mylar film were used to cover the window to allow X-ray beam penetration in transmission mode. A graphite disc was employed for the cathode side to apply uniform pressure to the whole Se electrode. A much thinner Ca foil (thickness: 0.004 ° , ESPI metals) was used for the operando cell to enable transmission mode XAS and XRD during in situ measurements.

2.5. DFT Calculations. Geometries were optimized using density functional theory calculations that were performed as implemented in the Vienna Ab Initio Simulation Package (VASP).^{27–29} The interactions between core and valence electrons were treated by the

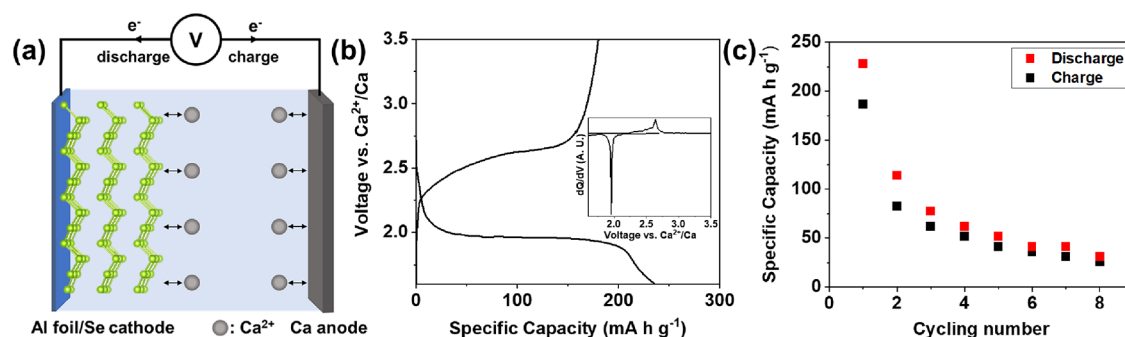


Figure 2. (a) Schematic of the Ca metal battery with a Se/AC cathode and Ca anode. (b) Galvanostatic discharge–charge curves of the Se cathode at 100 mA g^{-1} at room temperature. The inset shows a corresponding differential capacity plot for panel (b). (c) Cycling performance of the Se/AC cathode at 100 mA g^{-1} at room temperature.

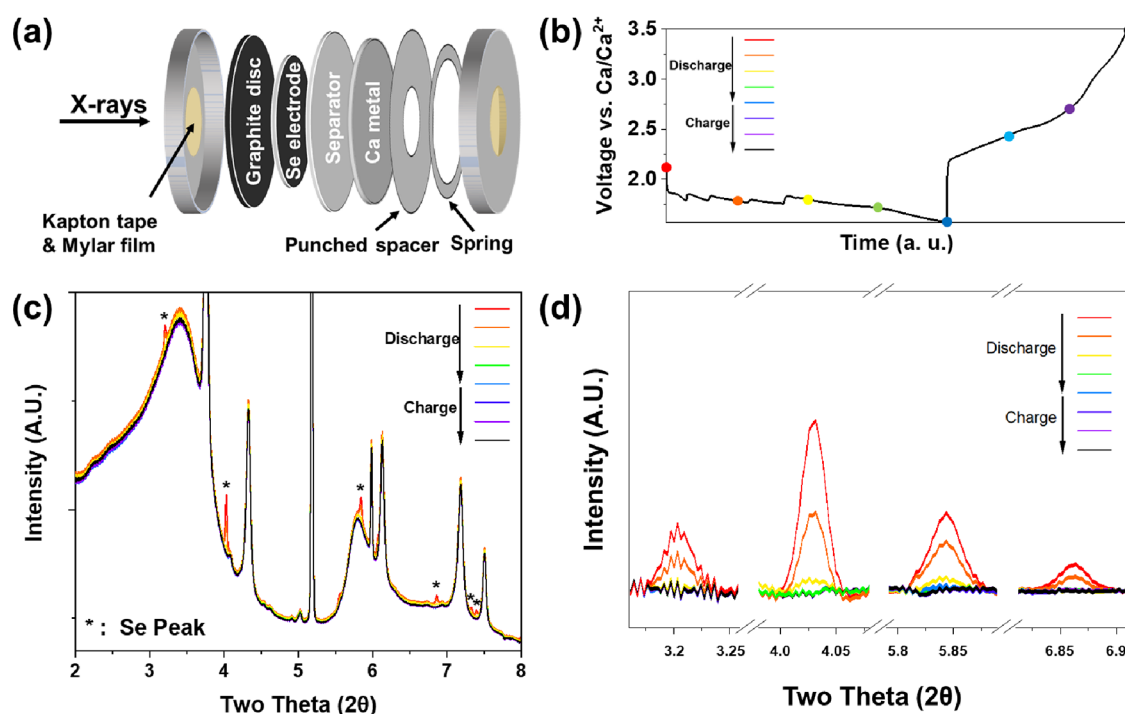


Figure 3. (a) Schematic of a coin cell used for operando measurement. (b) Voltage profile during in situ SXR D measurement. (c) Full in situ synchrotron XRD patterns measured during discharge and charge. (d) Magnified in situ SXR D patterns during discharge and charge. Background subtraction was performed for XRD patterns.

projector-augmented wave (PAW) potentials, and a plane-wave cutoff energy of 520 eV was used.^{30,31} The generalized gradient approximation (GGA) form of the electron exchange–correlation functional formulated by Perdew–Burke–Ernzerhof (PBE) was used.³² The unit cell geometries were relaxed for all structures with a force tolerance for the atom positions of 0.03 eV/Å using the conjugated gradient method.

3. RESULTS AND DISCUSSION

The electrolyte used was based on $\text{Ca}(\text{B}(\text{hfp})_4)_2$ in the DME solvent and was tested using cyclic voltammetry (CV) to verify its stability as an electrolyte for a calcium metal battery (Figure 1). CV data confirmed that reversible Ca plating and stripping both on Au (Figure 1a) and Ca (Figure 1b) working electrodes were present with low overpotential and was supportive of its use in a full cell configuration. The Se cathodes were evaluated versus a Ca metal anode using galvanostatic discharge–charge tests in 0.2 M $\text{Ca}(\text{B}(\text{hfp})_4)_2$ in DME. Se/activated carbon (AC) composite electrodes were used as working electrodes

instead of bulk Se powder to maintain contact with the conductive carbon matrix as the state of charge was varied. Reports from the Li and Na battery systems indicated that this composite formulation had higher Se utilization.^{33,34} By confining the Se within a conductive carbon matrix, smaller particle sizes are observed, which leads to an improvement in the reaction kinetics. Indeed, the bulk Se electrode prepared without using the AC platform showed poor electrochemical performances (Figure S1). Thermogravimetric analysis (TGA) was used to determine the selenium content (wt %) in the Se/AC composite (Figure S2a). The Se in the Se/AC composite began evaporating near 300 °C, resulting in a 40% weight loss by ~530 °C. The total loading of selenium was found to be approximately 40 wt %, and this figure was used for future calculations. The slight weight loss at high temperature was associated with the AC (Figure S2b).

Representative galvanostatic discharge–charge profiles of the Se/AC cathode and Ca metal anode battery (Figure 2a, Swagelok-type cell) are shown in Figure 2b. The Se/AC

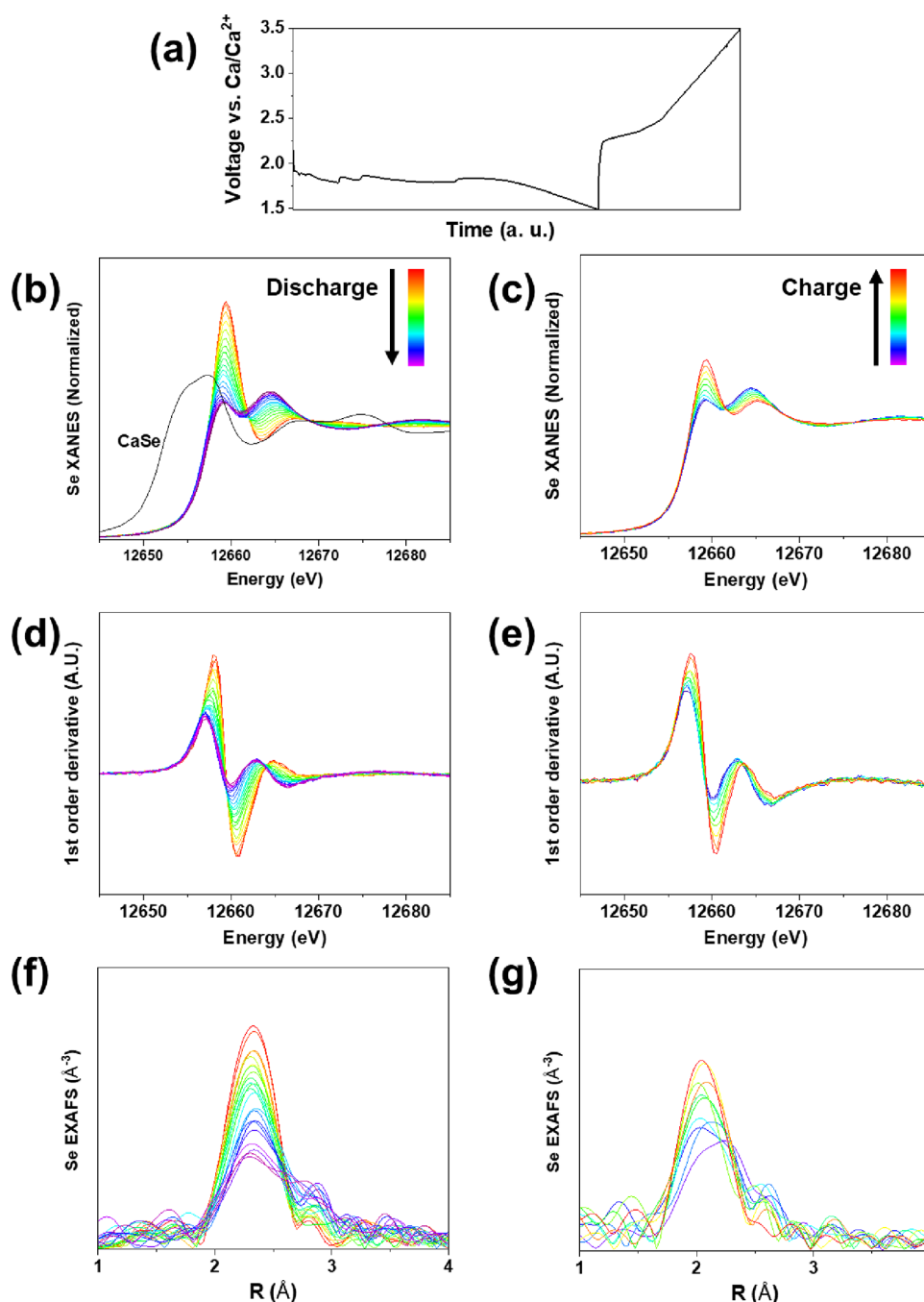


Figure 4. (a) Voltage profile during in situ XAS measurement. In situ Se K-edge XANES spectra during (b) discharge and (c) charge. The Se K-edge XANES spectrum of CaSe is plotted together in panel (b). Corresponding first-order derivative plots of in situ Se K-edge XANES spectra during (d) discharge and (e) charge. In situ Se K-edge EXAFS spectra during (f) discharge and (g) charge.

electrode delivered a first cycle discharge capacity of 235 mA h g^{-1} and charge capacity of 180 mA h g^{-1} at a current density of 100 mA g^{-1} , corresponding to an insertion of 0.35 and a removal of 0.27 mol of Ca^{2+}/Se , respectively. The electrode showed a well-defined discharge and charge plateau near 2.0 and 2.6 V (vs Ca^{2+}/Ca), respectively, in contrast to a previous report lacking a distinct voltage plateau, indicative of a significant capacitive contribution from the anode to the total capacity.²⁶ Based on the formation energy for hypothetical endmember CaSe (-2.26 eV/atom), the average voltage of the reaction $Ca + Se \leftrightarrow CaSe$ can be calculated to be 2.26 V (vs Ca^{2+}/Ca), which is close to the middle point of the discharge

and charge plateau (~ 2.3 V (vs Ca^{2+}/Ca)). In addition, the single voltage plateau in both the discharge and charge processes suggests that the redox reactions are a single-step reaction rather than multiple stepwise reactions. This is different from previous Se electrochemical studies where multiple voltage plateaus were observed.^{35,36} The redox reactions are confirmed in the dQ/dV curve with a difference between redox peaks of 0.68 V (Figure 2b). When the Se cathode was tested with a different type of Ca metal anode, it showed an even smaller hysteresis (~ 0.35 V), indicating that there is a contribution to the hysteresis from a Ca metal negative (Figure S3). This implies that hysteresis can be

decreased further by optimization of both the anode and cathode. While the voltage hysteresis is higher than the observed voltage hysteresis in the Li–Se system (0.1–0.2 V), it is comparable to other multivalent ion battery systems (Zn–Se and Mg–Se), which may indicate a charge transfer or that multivalent-ion diffusion-related phenomena are important to the mechanism.^{36–38} On cycling, the Se/AC electrode, when being evaluated at the same current density for several cycles, showed significant capacity decay (Figure 2c). Compared to reported sulfur-based systems, this has been attributed to cathode issues (e.g., dissolution and pulverization), anode surface passivation, or possibly a combination.^{10,11,18,39–41} The capacity decay problem will be discussed in this context and will be further investigated in the following studies.

Examining the Ca–Se reaction mechanism in more detail, the phase evolution of Se electrodes during cycling was investigated using in situ XRD. The punched coin cell design used for these operando studies is shown in Figure 3a. Figure 3b shows a voltage profile of the in situ coin cell during operando XRD measurements. Please note that the observed charge capacity of the in situ coin cell, used for this specific data collection, is slightly lower than the Swagelok cell typically used. The operando cell showed a slightly higher voltage hysteresis, probably due to a cell design that contains more components, which can increase contact resistances and thus the voltage potential. The full XRD patterns that are shown in Figure 3c,d are magnified XRD patterns during in situ measurements where any peak changes were observed. As Se reacts with Ca²⁺ ions, a decrease in Se peak intensity was observed. When the electrode was 50% discharged, the Se XRD peaks had mostly disappeared with no additional changes observed on further discharging or charging. Based on these observations, we hypothesize that the discharge and charge products formed under these conversion reactions are either amorphous or nanocrystalline and are not observed by XRD under the condition used. Similar observations have been reported in other conversion systems.^{42,43} Density functional theory (DFT) calculations were performed using several possible calcium selenide candidate structures, whose stoichiometries, between 1:1 and 1:4, are approximately in the range of observed specific capacities. Figure S5a shows formation energies of these calcium selenides, indicating that all intermediate phases between Se and CaSe turned out to be metastable. Therefore, according to the calculations, intermediate phases are unlikely to be in a crystalline form, which is also consistent with our XRD results.

To gain insight into the charge storage mechanism of the Se/AC electrode, the first cycle Se redox reactions and local structural changes were studied by in situ synchrotron XAS measurements. In situ XAS can be very meaningful, especially for amorphous phases where information from XRD is limited. Figure 4a shows the voltage profile from an in situ cell during operando XAS measurements. Figure 4b and Figure 4c present in situ Se K-edge X-ray absorption near-edge structure (XANES) spectra during discharge and charge, respectively, and the corresponding first-order derivative plots are shown in Figure 4d (discharge) and Figure 4e (charge). The selenium K-edge absorption occurs due to an electron transition from 1s states to unoccupied 4p states. Reversible changes in XANES spectra were observed during discharge and charge. The intensity of the white line peak decreases during discharge due to increased electron population of the valence 4p orbitals and vice versa during charge. The edge shift associated with Se

reduction and oxidation in Figure 4b,c appears small. The energy position of the edge can be determined as the lowest energy peak of the first derivative of the XANES spectra. In Figure 4d,e, it was confirmed that the Se K-edge shifted toward lower energies due to the reduction of Se and it shifted back toward high energies during charge. However, the fully charged state was not identical to its pristine state, indicating only partial reversibility and consistent with the first cycle electrochemical testing noted earlier. We suspect that this is related to the drop off noted in the charge capacity relative to discharge capacity (Figure 4a) and again may be related to in situ testing format. Further improvements in our coin cell setup will be made in the future. Of particular interest, the XANES spectra showed isosbestic points, suggesting that Se undergoes two-phase reactions during cycling. To examine the reaction mechanisms, the Se K-edge XANES spectrum of the hypothetical end product, CaSe, was measured (Figure 4b). The identification and purity of CaSe powder were confirmed by ex situ XRD (Figure S6). Interestingly, the Se K-edge XANES spectrum of CaSe was quite different from the in situ XANES spectra collected for the experimental samples and is shown in Figure 4b. This indicates that the fully calcinated material CaSe is likely not present under our experimental conditions, but it is likely to be an intermediate phase with composition CaSe_x ($x > 1$), which is consistent with the measured capacities. To learn more about the properties of the discharged cathode phases, the local environment around Se was studied using in situ extended X-ray absorption fine structure (EXAFS) spectra during cycling. Figure 4f and Figure 4g present in situ Se K-edge EXAFS spectra during discharge and charge, respectively. In the Fourier-transformed EXAFS, the peaks from 2 to 2.5 Å (the phase is not corrected) can be indexed to Se–Se first neighboring bonds and the peaks from 2.5 to 3 Å can be indexed to Se–Se second neighboring bonds. Partial reversibility in the local structure was observed in EXAFS spectra during cycling, which is consistent with XANES results.

EDS analysis was conducted on the electrode to confirm the extent of Ca insertion and extraction during cycling (Figure 5). Se/AC electrodes were washed with acetonitrile to ensure that no residue from the calcium electrolyte salt remained on the surface, even though there was a possibility of loss of active materials during washing. EDS spectra were normalized to the

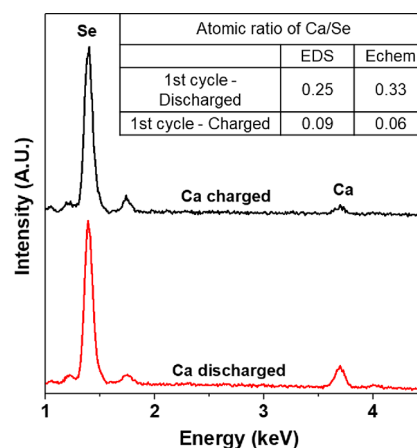


Figure 5. Ex situ EDS spectra of Se electrodes after discharge and charge in Ca cells and EDS results for Se electrodes. The table shows the atomic ratio of Ca/Se after discharge and charge.

Se signal. The discharged Se electrode showed Ca signals at 3.7 keV for Ca $K\alpha$ and 4.0 keV for Ca $K\beta$. After charging, the Ca signal decreased relative to the Se peak, supporting the removal of Ca relative to the discharged sample. The amount of Ca in electrodes, based on the EDS quantification results and calculated from the electrochemistry of EDS samples, is shown in an inset in Figure 5, and the trends are in rough agreement. While the data clearly show Ca ions being the active transporting species, consistent with the reported diagnostic evidence, the small discrepancy in the EDS results is probably due to the differences in sample history and a capacity fade mechanism that increases the complexity of the sample. After cycling, further EDS analysis of the separator and the discharged Ca metal anode were evaluated as points where selenium may become isolated. Unlike the case of Se electrodes, the separator and Ca metal anode were not washed with acetonitrile to avoid Se, if it is on the surface, being washed away. Selenium was detected on the separator as expected by the observed color change (Figure S7), suggesting that active material loss may be a contributing factor to the observed capacity decay. However, at the same time, no detectable Se signal was observed on the Ca metal, indicating that Se_x^{-2} anions do not travel across the cell and react with calcium metal (shuttling mechanism). This is consistent with the observation that the discharge capacity was higher than the charge capacity. A consequence of the shuttle mechanism is that charge capacity is higher than discharge capacity.

4. CONCLUSIONS

In conclusion, elemental selenium has been evaluated as a conversion cathode in a Ca-ion cell and studied using a Ca metal anode in a non-aqueous Ca-based electrolyte. This study finds that the Se electrode is quasi-reversibly converted to Ca_xSe during cell discharge ($x \approx 0.3$) and exhibited an initial discharge capacity of 235 mA h g^{-1} at 100 mA g^{-1} with a discharge plateau around 2.0 V (vs Ca^{2+}/Ca). The Se cathode showed well-defined voltage plateaus and a moderate voltage hysteresis as compared to typical multivalent battery electrodes. Based on operando synchrotron XRD, XAS, and EDS results, we have confirmed that the full cell electrochemical reaction between Se and Ca is reversible. Future studies will identify conditions to increase specific capacity, decrease voltage hysteresis, and improve cyclability. We believe that this work demonstrates that Se-based electrodes are promising CIB cathodes and will spur further research on other chalcogens as cathode materials for CIBs.

■ ASSOCIATED CONTENT

SI Supporting Information

The Supporting Information is available free of charge at <https://pubs.acs.org/doi/10.1021/acs.chemmater.2c03343>.

Galvanostatic discharge–charge curves of the bulk Se cathode, thermogravimetric analysis for Se/AC and AC, galvanostatic discharge–charge curves of the Se cathode tested using a different type of Ca metal, galvanostatic discharge–charge curves of Figure 2c, formation energies of possible calcium selenide candidates by DFT calculations, XRD pattern of CaSe, and photograph of a used separator (PDF)

■ AUTHOR INFORMATION

Corresponding Authors

Sanghyeon Kim – Chemical Sciences and Engineering Division and Joint Center for Energy Storage Research, Argonne National Laboratory, Lemont, Illinois 60439, United States; Department of Materials Science and Engineering, Inha University, Incheon 22212, Republic of Korea; orcid.org/0000-0003-2789-449X; Email: sanghyeon.kim@anl.gov

John T. Vaughan – Chemical Sciences and Engineering Division and Joint Center for Energy Storage Research, Argonne National Laboratory, Lemont, Illinois 60439, United States; orcid.org/0000-0002-2556-6129; Email: vaughney@anl.gov

Authors

Nathan T. Hahn – Joint Center for Energy Storage Research, Argonne National Laboratory, Lemont, Illinois 60439, United States; Material, Physical and Chemical Sciences Center, Sandia National Laboratories, Albuquerque, New Mexico 87185, United States; orcid.org/0000-0001-6187-4068

Timothy T. Fister – Chemical Sciences and Engineering Division and Joint Center for Energy Storage Research, Argonne National Laboratory, Lemont, Illinois 60439, United States; orcid.org/0000-0001-6537-6170

Noel J. Leon – Chemical Sciences and Engineering Division and Joint Center for Energy Storage Research, Argonne National Laboratory, Lemont, Illinois 60439, United States

Xiao-Min Lin – Center for Nanoscale Materials, Argonne National Laboratory, Lemont, Illinois 60439, United States; orcid.org/0000-0002-2879-3474

Haesun Park – Joint Center for Energy Storage Research and Materials Science Division, Argonne National Laboratory, Lemont, Illinois 60439, United States; School of Integrative Engineering, Chung-Ang University, Seoul 06974, Republic of Korea

Peter Zapol – Joint Center for Energy Storage Research and Materials Science Division, Argonne National Laboratory, Lemont, Illinois 60439, United States; orcid.org/0000-0003-0570-9169

Saul H. Lapidus – Joint Center for Energy Storage Research and X-ray Science Division, Advanced Photon Source, Argonne National Laboratory, Lemont, Illinois 60439, United States; orcid.org/0000-0002-7486-4325

Chen Liao – Chemical Sciences and Engineering Division and Joint Center for Energy Storage Research, Argonne National Laboratory, Lemont, Illinois 60439, United States; orcid.org/0000-0001-5168-6493

Complete contact information is available at:

<https://pubs.acs.org/10.1021/acs.chemmater.2c03343>

Notes

The authors declare no competing financial interest.

■ ACKNOWLEDGMENTS

This work was supported by the Joint Center for Energy Storage Research, an energy innovation hub funded by the U.S. Department of Energy, Office of Science, Basic Energy Sciences. This research used resources of the Advanced Photon Source, a U.S. Department of Energy (DOE) Office of Science user facility operated for the DOE Office of Science by Argonne National Laboratory under contract no. DE-AC02-

06CH11357. MRCAT operations are supported by the Department of Energy and the MRCAT member institutions. This research used resources of the Advanced Photon Source, a U.S. Department of Energy (DOE) Office of Science user facility operated for the DOE Office of Science by Argonne National Laboratory under contract no. DE-AC02-06CH11357. This work is conducted at Argonne National Laboratory supported by the U.S. Department of Energy under contract DE-A02-06CH11357. The use of the Center for Nanoscale Materials, an Office of Science user facility, was supported by the U.S. Department of Energy, Office of Science, Office of Basic Energy Sciences, under contract no. DE-AC02-06CH11357. Sandia National Laboratories is a multimission laboratory managed and operated by the National Technology & Engineering Solutions of Sandia, LLC, a wholly owned subsidiary of Honeywell International Inc., for the U.S. Department of Energy's National Nuclear Security Administration under contract DE-NA0003525. This paper describes objective technical results and analysis. Any subjective views or opinions that might be expressed in the paper do not necessarily represent the views of the U.S. Department of Energy or the U.S. government.

REFERENCES

- (1) Blomgren, G. E. The Development and Future of Lithium Ion Batteries. *J. Electrochem. Soc.* **2016**, *164*, A5019–A5025.
- (2) Etacheri, V.; Marom, R.; Elazari, R.; Salitra, G.; Aurbach, D. Challenges in the development of advanced Li-ion batteries: a review. *Energy Environ. Sci.* **2011**, *4*, 3243–3262.
- (3) Canepa, P.; Sai Gautam, G.; Hannah, D. C.; Malik, R.; Liu, M.; Gallagher, K. G.; Persson, K. A.; Ceder, G. Odyssey of Multivalent Cathode Materials: Open Questions and Future Challenges. *Chem. Rev.* **2017**, *117*, 4287–4341.
- (4) Ponrouch, A.; Bitenc, J.; Dominko, R.; Lindahl, N.; Johansson, P.; Palacin, M. R. Multivalent rechargeable batteries. *Energy Storage Mater.* **2019**, *20*, 253–262.
- (5) Liu, M.; Rong, Z.; Malik, R.; Canepa, P.; Jain, A.; Ceder, G.; Persson, K. A. Spinel compounds as multivalent battery cathodes: a systematic evaluation based on ab initio calculations. *Energy Environ. Sci.* **2015**, *8*, 964–974.
- (6) Ponrouch, A.; Palacin, M. R. On the road toward calcium-based batteries. *Curr. Opin. Electrochem.* **2018**, *9*, 1–7.
- (7) Gummow, R. J.; Vamvounis, G.; Kannan, M. B.; He, Y. Calcium-Ion Batteries: Current State-of-the-Art and Future Perspectives. *Adv. Mater.* **2018**, *30*, No. 1801702.
- (8) Ponrouch, A.; Frontera, C.; Barde, F.; Palacin, M. R. Towards a calcium-based rechargeable battery. *Nat. Mater.* **2016**, *15*, 169–172.
- (9) Wang, D.; Gao, X.; Chen, Y.; Jin, L.; Kuss, C.; Bruce, P. G. Plating and stripping calcium in an organic electrolyte. *Nat. Mater.* **2018**, *17*, 16–20.
- (10) Li, Z.; Fuhr, O.; Fichtner, M.; Zhao-Karger, Z. Towards stable and efficient electrolytes for room-temperature rechargeable calcium batteries. *Energy Environ. Sci.* **2019**, *12*, 3496–3501.
- (11) Shyamsunder, A.; Blanc, L. E.; Assoud, A.; Nazar, L. F. Reversible Calcium Plating and Stripping at Room Temperature Using a Borate Salt. *ACS Energy Lett.* **2019**, *4*, 2271–2276.
- (12) Jie, Y.; Tan, Y.; Li, L.; Han, Y.; Xu, S.; Zhao, Z.; Cao, R.; Ren, X.; Huang, F.; Lei, Z.; Tao, G.; Zhang, G.; Jiao, S. Electrolyte Solvation Manipulation Enables Unprecedented Room-Temperature Calcium-Metal Batteries. *Angew. Chem., Int. Ed.* **2020**, *59*, 12689–12693.
- (13) Li, Z.; Vinayan, B. P.; Diemant, T.; Behm, R. J.; Fichtner, M.; Zhao-Karger, Z. Rechargeable Calcium-Sulfur Batteries Enabled by an Efficient Borate-Based Electrolyte. *Small* **2020**, *16*, No. 2001806.
- (14) Scafuri, A.; Berthelot, R.; Pirnat, K.; Vizintin, A.; Bitenc, J.; Aquilanti, G.; Foix, D.; Dedryvère, R.; Arçon, I.; Dominko, R.; Stievano, L. Spectroscopic Insights into the Electrochemical Mechanism of Rechargeable Calcium/Sulfur Batteries. *Chem. Mater.* **2020**, *32*, 8266–8275.
- (15) Li, Z.; Vinayan, B. P.; Jankowski, P.; Njel, C.; Roy, A.; Vegge, T.; Maibach, J.; Lastra, J. M. G.; Fichtner, M.; Zhao-Karger, Z. Multi-Electron Reactions Enabled by Anion-Based Redox Chemistry for High-Energy Multivalent Rechargeable Batteries. *Angew. Chem., Int. Ed.* **2020**, *59*, 11483–11490.
- (16) Bitenc, J.; Scafuri, A.; Pirnat, K.; Lozinšek, M.; Jerman, I.; Grdadolnik, J.; Fraisse, B.; Berthelot, R.; Stievano, L.; Dominko, R. Electrochemical Performance and Mechanism of Calcium Metal-Organic Battery. *Batteries Supercaps* **2020**, *4*, 214–220.
- (17) Yu, X.; Boyer, M. J.; Hwang, G. S.; Manthiram, A. Toward a Reversible Calcium-Sulfur Battery with a Lithium-Ion Mediation Approach. *Adv. Energy Mater.* **2019**, *9*, No. 1803794.
- (18) Kisu, K.; Kim, S.; Shinohara, T.; Zhao, K.; Zuttel, A.; Orimo, S. I. Monocarborane cluster as a stable fluorine-free calcium battery electrolyte. *Sci. Rep.* **2021**, *11*, 7563.
- (19) Gao, T.; Hou, S.; Wang, F.; Ma, Z.; Li, X.; Xu, K.; Wang, C. Reversible S^0/MgS_x Redox Chemistry in a $MgTFSI_2/MgCl_2/DME$ Electrolyte for Rechargeable Mg/S Batteries. *Angew. Chem., Int. Ed.* **2017**, *56*, 13526–13530.
- (20) Wang, W.; Yuan, H.; NuLi, Y.; Zhou, J.; Yang, J.; Wang, J. Sulfur@microporous Carbon Cathode with a High Sulfur Content for Magnesium–Sulfur Batteries with Nucleophilic Electrolytes. *J. Phys. Chem. C* **2018**, *122*, 26764–26776.
- (21) Yu, X.; Manthiram, A. Performance Enhancement and Mechanistic Studies of Magnesium–Sulfur Cells with an Advanced Cathode Structure. *ACS Energy Lett.* **2016**, *1*, 431–437.
- (22) Du, A.; Zhang, Z.; Qu, H.; Cui, Z.; Qiao, L.; Wang, L.; Chai, J.; Lu, T.; Dong, S.; Xu, H.; Zhou, X.; Cui, G. An efficient organic magnesium borate-based electrolyte with non-nucleophilic characteristics for magnesium–sulfur battery. *Energy Environ. Sci.* **2017**, *10*, 2616–2625.
- (23) Zeng, L.; Zeng, W.; Jiang, Y.; Wei, X.; Li, W.; Yang, C.; Zhu, Y.; Yu, Y. A Flexible Porous Carbon Nanofibers-Selenium Cathode with Superior Electrochemical Performance for Both Li-Se and Na-Se Batteries. *Adv. Energy Mater.* **2015**, *5*, No. 1401377.
- (24) Eftekhari, A. The rise of lithium–selenium batteries. *Sustainable Energy Fuels* **2017**, *1*, 14–29.
- (25) Cui, Y.; Abouimrane, A.; Sun, C. J.; Ren, Y.; Amine, K. Li-Se battery: absence of lithium polyselenides in carbonate based electrolyte. *Chem. Comm.* **2014**, *50*, 5576–5579.
- (26) Zhou, R.; Hou, Z.; Liu, Q.; Du, X.; Huang, J.; Zhang, B. Unlocking the Reversible Selenium Electrode for Non-Aqueous and Aqueous Calcium-Ion Batteries. *Adv. Funct. Mater.* **2022**, *32*, No. 2200929.
- (27) Kresse, G.; Furthmüller, J. Efficient iterative schemes for ab initio total-energy calculations using a plane-wave basis set. *Phys. Rev. B* **1996**, *54*, 11169–11186.
- (28) Kresse, G.; Furthmüller, J. Efficiency of ab-initio total energy calculations for metals and semiconductors using a plane-wave basis set. *Comput. Mater. Sci.* **1996**, *6*, 15–50.
- (29) Kresse, G.; Hafner, J. Ab initio molecular dynamics for liquid metals. *Phys. Rev. B* **1993**, *47*, 558–561.
- (30) Blochl, P. E. Projector augmented-wave method. *Phys. Rev. B* **1994**, *50*, 17953–17979.
- (31) Kresse, G.; Joubert, D. From ultrasoft pseudopotentials to the projector augmented-wave method. *Phys. Rev. B* **1999**, *59*, 1758–1775.
- (32) Perdew, J. P.; Burke, K.; Ernzerhof, M. Generalized Gradient Approximation Made Simple. *Phys. Rev. Lett.* **1996**, *77*, 3865–3868.
- (33) Yang, C. P.; Yin, Y. X.; Guo, Y. G. Elemental Selenium for Electrochemical Energy Storage. *J. Phys. Chem. Lett.* **2015**, *6*, 256–266.
- (34) Li, S.; Yang, H.; Xu, R.; Jiang, Y.; Gong, Y.; Gu, L.; Yu, Y. Selenium embedded in MOF-derived N-doped microporous carbon polyhedrons as a high performance cathode for sodium–selenium batteries. *Mater. Chem. Front.* **2018**, *2*, 1574–1582.

(35) Cui, Y.; Abouimrane, A.; Lu, J.; Bolin, T.; Ren, Y.; Weng, W.; Sun, C.; Maroni, V. A.; Heald, S. M.; Amine, K. (De)lithiation mechanism of Li/SeS_x ($x = 0-7$) batteries determined by in-situ synchrotron X-ray diffraction and X-ray absorption spectroscopy. *J. Am. Chem. Soc.* **2013**, *135*, 8047–8056.

(36) Chen, Z.; Mo, F.; Wang, T.; Yang, Q.; Huang, Z.; Wang, D.; Liang, G.; Chen, A.; Li, Q.; Guo, Y.; Li, X.; Fan, J.; Zhi, C. Zinc/selenium conversion battery: a system highly compatible with both organic and aqueous electrolytes. *Energy Environ. Sci.* **2021**, *14*, 2441–2450.

(37) Zhang, Z.; Chen, B.; Xu, H.; Cui, Z.; Dong, S.; Du, A.; Ma, J.; Wang, Q.; Zhou, X.; Cui, G. Self-Established Rapid Magnesiumation/De-Magnesiumation Pathways in Binary Selenium-Copper Mixtures with Significantly Enhanced Mg-Ion Storage Reversibility. *Adv. Funct. Mater.* **2018**, *28*, No. 1701718.

(38) Zhang, Z.; Cui, Z.; Qiao, L.; Guan, J.; Xu, H.; Wang, X.; Hu, P.; Du, H.; Li, S.; Zhou, X.; Dong, S.; Liu, Z.; Cui, G.; Chen, L. Novel Design Concepts of Efficient Mg-Ion Electrolytes toward High-Performance Magnesium-Selenium and Magnesium-Sulfur Batteries. *Adv. Energy Mater.* **2017**, *7*, No. 1602055.

(39) Nielson, K. V.; Luo, J.; Liu, T. L. Optimizing Calcium Electrolytes by Solvent Manipulation for Calcium Batteries. *Batteries Supercaps* **2020**, *3*, 766–772.

(40) Forero-Saboya, J.; Bodin, C.; Ponrouch, A. A Boron-based Electrolyte Additive for Calcium Electrodeposition. *Electrochem. Commun.* **2021**, *124*, No. 106936.

(41) Leon, N. J.; Xie, X.; Yang, M.; Driscoll, D. M.; Connell, J. G.; Kim, S.; Seguin, T.; Vaughey, J. T.; Balasubramanian, M.; Persson, K. A.; Liao, C. Room-Temperature Calcium Plating and Stripping Using a Perfluoroalkoxyaluminate Anion Electrolyte. *J. Phys. Chem. C* **2022**, *126*, 13579–13584.

(42) Kim, S.; Choi, J.; Bak, S. M.; Sang, L.; Li, Q.; Patra, A.; Braun, P. V. Reversible Conversion Reactions and Small First Cycle Irreversible Capacity Loss in Metal Sulfide-Based Electrodes Enabled by Solid Electrolytes. *Adv. Funct. Mater.* **2019**, *29*, No. 1901719.

(43) Li, Q.; Liu, H.; Yao, Z.; Cheng, J.; Li, T.; Li, Y.; Wolverton, C.; Wu, J.; Dravid, V. P. Electrochemistry of Selenium with Sodium and Lithium: Kinetics and Reaction Mechanism. *ACS Nano* **2016**, *10*, 8788–8795.

Recommended by ACS

Long-Cycle-Life Calcium Battery with a High-Capacity Conversion Cathode Enabled by a Ca²⁺/Li⁺ Hybrid Electrolyte

Zhen Meng, Zhirong Zhao-Karger, *et al.*

DECEMBER 04, 2022
ACS APPLIED MATERIALS & INTERFACES

READ 

Exploration of NaSICON Frameworks as Calcium-Ion Battery Electrodes

Dereje Bekele Tekliye, Gopalakrishnan Sai Gautam, *et al.*

NOVEMBER 11, 2022
CHEMISTRY OF MATERIALS

READ 

Polyimides as Promising Cathodes for Metal–Organic Batteries: A Comparison between Divalent (Ca²⁺, Mg²⁺) and Monovalent (Li⁺, Na⁺) Cations

Damien Monti, Alexandre Ponrouch, *et al.*

JUNE 27, 2023
ACS APPLIED ENERGY MATERIALS

READ 

Highly Reversible Intercalation of Calcium Ions in Layered Vanadium Compounds Enabled by Acetonitrile–Water Hybrid Electrolyte

Xiaolu Qin, Baohua Li, *et al.*

JUNE 20, 2023
ACS NANO

READ 

Get More Suggestions >